ISSN 0016-7037
Volume 75, Number 4
February 15, 2011

Geochimica et Cosmochimica Acta

JOURNAL OF THE GEOCHEMICAL SOCIETY
AND THE METEORITICAL SOCIETY

Volume 75, Number 4 February 15, 2011

Articles

Continued on outside back cover

Available online at www.sciencedirect.com
ScienceDirect
Geochimica et Cosmochimica Acta 75 (2011) 951–964
Geochimica et Cosmochimica Acta
www.elsevier.com/locate/gca

Combined microthermometric and Raman spectroscopic technique to determine the salinity of H_2O–CO_2–NaCl fluid inclusions based on clathrate melting

András Fall [a,*], Brian Tattitch [b], Robert J. Bodnar [a]

[a] Fluids Research Laboratory, Department of Geosciences, Virginia Tech, Blacksburg, VA 24061, USA
[b] Laboratory for Mineral Deposits Research, Department of Geology, University of Maryland, College Park, MD 20742, USA

Received 29 July 2010; accepted in revised form 27 November 2010; available online 4 December 2010

Abstract

Fluid inclusions approximated by the system H_2O–CO_2–NaCl are common in many geologic environments. In order to apply microthermometric data from these inclusions to infer P–T (pressure–temperature) trapping conditions, the composition of the inclusions, including the salinity, must be known. Normally, salinities of aqueous inclusions are determined from ice-melting temperatures obtained during microthermometry. However, when CO_2-bearing aqueous fluid inclusions are cooled they often form a hydrate that incorporates H_2O into the structure, and salinities estimated from ice-melting temperatures are therefore higher than the actual salinity. A technique that combines data from Raman spectroscopic and microthermometric analyses of individual inclusions was developed to determine the salinity of CO_2-bearing aqueous inclusions based on measured clathrate melting temperatures and CO_2 pressures obtained from Raman analyses. In this study, the pressure within inclusions was determined using Raman spectroscopy based on the splitting of the Fermi diad of CO_2, measured at the clathrate melting temperature. The CO_2 densities (and pressures) predicted by the equation developed in this study are in relatively good agreement with previously published equations, except for very low densities and correspondingly low pressures. The combined Raman spectroscopy – microthermometry technique thus provides both the temperature and the pressure in the inclusion at clathrate melting. For inclusions in which the clathrate melts in the presence of CO_2 liquid, the salinity can be determined with a precision of a few tenths of a wt% NaCl, whereas for inclusions in which clathrate melts in the presence of CO_2 vapor the salinity error may be a few wt% NaCl. Applying the method to synthetic fluid inclusions with known salinity suggests that the technique is valid for determining salinity of H_2O–CO_2–NaCl fluid inclusions in which clathrate melts in the presence of liquid CO_2 only or vapor CO_2 only.

1. INTRODUCTION

Fluid inclusions provide one of the best tools available to constrain the pressure, temperature and fluid composition (P–T–X) history of geological processes (Roedder, 1984). Microthermometry is the most commonly used technique to study fluid inclusions, and interpretation of fluid inclusion microthermometric data requires information on the P–T–X properties of model fluid systems that approximate the compositions of natural fluids. Fluids approximated by the system H_2O–CO_2–NaCl are common in many different geologic environments, including hydrothermal ore deposits (Roedder, 1984; Bodnar, 1995; Roedder and Bodnar, 1997) and medium- to high-grade metamorphic rocks (Crawford, 1981; Touret, 1981, 2001; Roedder, 1984). One of the more diagnostic characteristics of natural fluids for inferring source regions and processes is the salinity of the fluid (Yardley and Graham, 2002), and the salinity of gas-free fluid inclusions is usually determined by

* Corresponding author. Present address: Bureau of Economic Geology, Jackson School of Geosciences, The University of Texas at Austin, Austin, TX 78713, USA.
E-mail address: andras.fall@beg.utexas.edu (A. Fall).

0016-7037/$ - see front matter © 2010 Elsevier Ltd. All rights reserved.
doi:10.1016/j.gca.2010.11.021

comparing the ice-melting temperatures with experimental data that relate salinity and freezing point depression (Bodnar, 1993, 2003). However, if a volatile component such as CO_2 is present, a hydrate (clathrate) phase may form when the inclusions are cooled (Roedder, 1963) (Fig. 1). Generally, the hydrate is stable at temperatures higher than the ice-melting temperature and the ice melting event is obscured optically by the presence of hydrate, often preventing accurate determination of the temperature of ice melting. More importantly, because the hydrate incorporates H_2O into its structure and rejects salts and ions from its lattice (Sloan and Koh, 2008), salinities of the aqueous phase estimated from ice-melting temperatures are higher than the actual salinity of the aqueous phase if ice melting occurs before the hydrate melts. As a result, salinities of gas-bearing fluid inclusions cannot be determined directly from the ice-melting temperature (Roedder, 1963; Takenouchi and Kennedy, 1965; Collins, 1979). For this reason, Takenouchi and Kennedy (1965) proposed that the clathrate melting temperatures should be used to determine the salinity of CO_2-bearing fluid inclusions. Based on the experimental data of Chen (1972) and Bozzo et al. (1973, 1975), other workers, including Collins (1979) and Diamond (1992, 1994, 2003), extended the proposed method to a wider range of compositions, and today the method is routinely used to determine the salinity of fluid inclusions that contain CO_2 and/or other volatile components.

Clathrate stability in the H_2O–CO_2–NaCl system is a function of the temperature, CO_2 pressure and salinity. In the H_2O–CO_2 binary system, clathrate melts in the presence of liquid CO_2, vapor CO_2, and liquid H_2O (Fig. 1a–c) at the invariant quadruple point Q_2 at +10 °C (Fig. 2), but clathrate can also melt in the presence of liquid H_2O and either CO_2 vapor (Fig. 1d–f) or CO_2 liquid (Fig. 1g–i) if the pressure at the moment of clathrate melting is not on the CO_2 liquid–vapor curve. Chen (1972) and Bozzo et al. (1975) observed that adding salt to H_2O–CO_2 solutions shifts the quadruple invariant point Q_2 to lower temperatures and pressures (Fig. 2) in a manner similar to the way in which the triple point (ice + liquid + vapor) in the system H_2O–NaCl moves to lower temperatures (and pressures) with increasing salinity (Bodnar et al., 1985a; Bodnar, 1993). Because clathrate stability in the H_2O–CO_2–NaCl system is a function of pressure, temperature and salinity, determining the salinity of aqueous-carbonic inclusions requires knowledge of both the pressure and the temperature within the inclusion at the moment of clathrate melting. The temperature in an H_2O–CO_2–NaCl fluid inclusion is easily

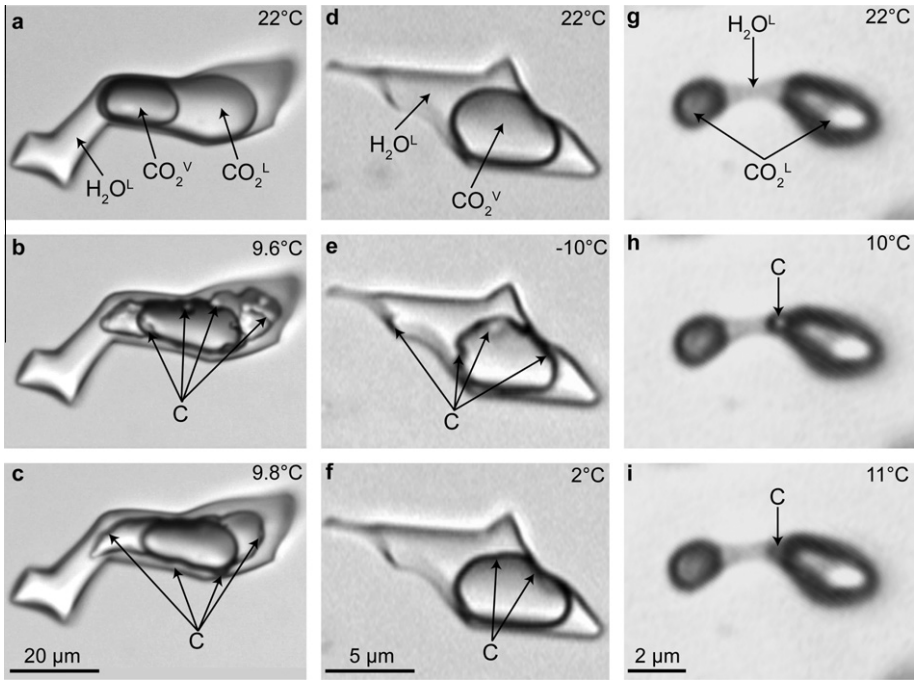

Fig. 1. Microthermometric behavior of H_2O–CO_2 synthetic fluid inclusions (SFI) containing various concentrations of CO_2 and having different CO_2 densities and homogenization behavior. (a–c): SFI containing 25 mol% CO_2. At room temperature ("a", 22 °C) the inclusion contains liquid H_2O, liquid CO_2 and CO_2 vapor. When the inclusion is cooled to low temperature it nucleates CO_2 clathrate and ice, and during heating the ice phase melts first leaving CO_2 clathrate as the only solid phase. The clathrate occurs at the interface between the aqueous phase and the CO_2 phase ("b"; 9.6 °C). The clathrate is still visible in the inclusion at 9.8 °C ("c"), which is close to the clathrate dissociation temperature of 10 °C. In this inclusion, clathrate melts in the presence of both liquid and vapor CO_2. (d–f): SFI containing 5 mol% CO_2. At room temperature ("d"; 22 °C) the inclusion contains two phases, liquid H_2O and vapor CO_2. When cooled, clathrate nucleates at the liquid H_2O–CO_2 vapor interface and is recognizable at −10 °C ("e") based on the irregular boundary of the CO_2 bubble. At 2 °C, close to the clathrate melting temperature of 2.8 °C ("f") slight distortion of the interface suggests that clathrate is still present. In this inclusion, clathrate melts in the presence of CO_2 vapor only. (g–i): SFI containing 87.5 mol% CO_2. At room temperature ("g"; 22 °C) the inclusion contains liquid H_2O and liquid CO_2. During cooling CO_2 clathrate nucleates at the liquid H_2O–liquid CO_2 interface and is still present at +10 °C ("h"); at 11 °C ("i") the clathrate is still visible. Final melting occurred at 14.8 °C in the presence of CO_2 liquid only.

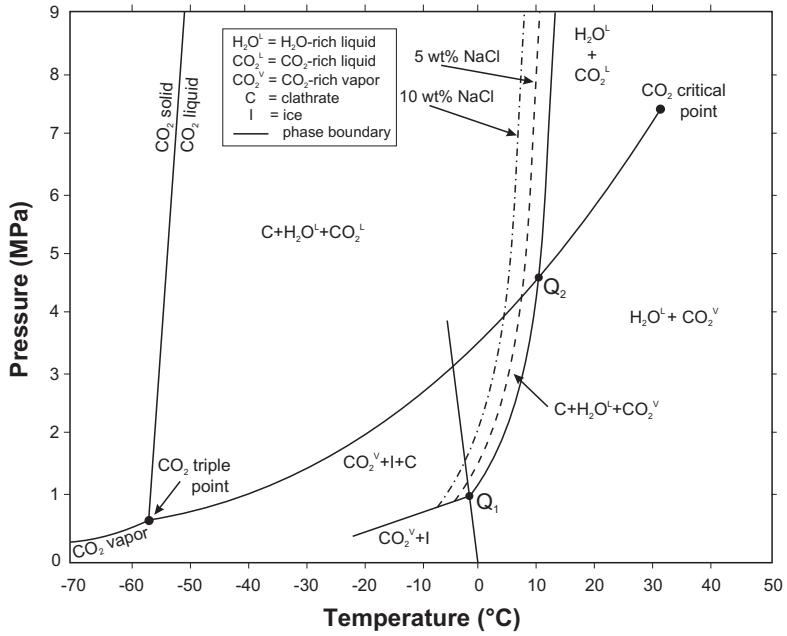

Fig. 2. Pressure–temperature phase diagram of the system H_2O–CO_2–NaCl at low temperatures. Solid lines represent phase boundaries for pure CO_2 and for H_2O–CO_2 based on data of Larson (1955). Dashed and dash-dot lines represent the CO_2 clathrate stability curves for clathrate in equilibrium with aqueous solutions having salinities of 5 and 10 wt% NaCl, respectively, based on experimental data of Chen (1972). At quadruple point Q_1 the four phases aqueous liquid, CO_2 vapor, CO_2 clathrate and H_2O ice (solid) coexist. At quadruple point Q_2 the four phases aqueous liquid, CO_2 vapor, CO_2 liquid, and CO_2 clathrate coexist.

determined using a microscope-mounted heating/cooling stage that records the temperature during heating and cooling, but the pressure in the fluid inclusion at the moment of clathrate melting cannot be measured directly (e.g., Dubessy et al., 1992). However, the pressure in the inclusion at the moment of clathrate melting in the system H_2O–$CO_2 \pm$ NaCl is known if clathrate melts in the presence of both liquid and vapor CO_2 because the P–T conditions at clathrate melting must be on the CO_2 liquid–vapor curve (point Q_2 on Fig. 2). Thus, most previous studies that report inclusion salinity based on the clathrate melting temperature are for inclusions in which the clathrate melts on the CO_2 liquid–vapor curve, or at the invariant point Q_2, and equations that relate clathrate melting temperature and salinity are only valid for inclusions in which clathrate melts at an invariant point Q_2 (e.g., Darling, 1991).

The P–T conditions of the invariant point Q_2 for compositions in the system H_2O–CO_2–NaCl were first determined by Chen (1972) in the range +10 to 0 °C (corresponding to 0–16 wt% NaCl). Bozzo et al. (1975) presented an equation to estimate salinity based on the clathrate melting temperature over the range +10 to 0 °C. Darling (1991) noted that the equation of Bozzo et al. (1975) worked well in the temperature range +10° to 0 °C, but could not be extended to lower temperatures to include the complete temperature (and composition) range over which clathrate melting occurs in the presence of saline aqueous solutions (+10 to −10 °C, corresponding to 0–24.2 wt% NaCl). For this reason, Darling (1991) developed a new equation that is valid at the Q_2 invariant point from +10 to −10 °C by combining the experimental data of Chen (1972) and Bozzo et al. (1975). The equation of Darling (1991) is thus valid for all salinities between 0 and the eutectic salinity, 24.2 wt% NaCl, provided that the clathrate phase melts in the presence of both liquid and vapor CO_2.

While many natural fluid inclusions do show clathrate melting in the presence of both liquid and vapor CO_2, clathrate may also dissociate (melt) in the presence of CO_2 vapor only or in the presence of CO_2 liquid only. However, the methods and equations summarized above are only valid along the CO_2 liquid–vapor curve and cannot be used to estimate salinity for these inclusions. To address this problem, Diamond (1992) developed a series of equations that estimate salinities of aqueous-carbonic inclusions in which clathrate melts at a temperature higher than the temperature of homogenization of the CO_2 phases, i.e., in the presence of liquid CO_2 only or CO_2 vapor only. The equations of Diamond (1992) require as input both the CO_2 homogenization temperature and the clathrate melting temperature, and the pressure within the inclusions is estimated based on the intersection of the CO_2 isochore with the clathrate melting temperature. The model assumes that the changing solubility of CO_2 in the aqueous phase and the continuous melting of clathrate over the P–T range between the CO_2 homogenization temperature and the clathrate melting temperature do not significantly affect the P–T location of the CO_2 isochore, and this is likely a valid assumption over a limited P–T range. In this paper we describe a technique that combines Raman spectrometry and microthermometry to determine the salinity of CO_2-bearing-aqueous fluid inclusions.

The Raman spectrum of CO_2 shows systematic variation as a function of the CO_2 density and offers the possibility to independently determine the pressure in an

H_2O–CO_2–NaCl fluid inclusion, as described below (modified from Rosso and Bodnar, 1995). The linear CO_2 molecule has four modes of vibration: a symmetric stretching mode (v_1), an antisymmetric stretching mode (v_3), and two bending modes (v_{2a} and v_{2b}) that have the same frequency and form a degenerate pair. According to Gordon and McCubbin (1966) the symmetric stretching mode occurs at 1332.87 cm^{-1} and this mode has nearly the same energy as the second excited state of an infrared active bending mode, v_2. Because they have nearly the same energy and the same symmetry species, they perturb each other in the excited state by a process known as Fermi resonance (Fermi, 1931). Fermi resonance causes the excited admixed states to split into two strong CO_2 lines referred to as the Fermi diad, with nominal frequencies of 1388.2 cm^{-1} (v_+; Fig. 3) and 1285.4 cm^{-1}(v_-; Fig. 3). The distance between the two peaks of the Fermi diad (splitting) of CO_2 (Fig. 3) is density (pressure) dependent (Wright and Wang, 1973, 1975). In this study, we determined the relationship between the Fermi diad splitting and CO_2 density over the range −10 °C to +35 °C and used this relationship to determine the density of the CO_2 phase present in the inclusion at the clathrate melting temperature. Then, using an equation of state for CO_2, the pressure corresponding to the measured temperature and calculated CO_2 density was determined. The results were compared to previously published experimental data and numerical models that predict salinity based on clathrate melting temperature along the CO_2 L–V curve to confirm that the method described here can be used to estimate the salinity of H_2O–CO_2–NaCl fluid inclusions. The method described here represents an extension of earlier studies that applied the density-dependence of the splitting of the Fermi diad of CO_2 to develop a "densimeter" for CO_2 fluid inclusions (Kawakami et al., 2003; Yamamoto and Kagi, 2006; Song et al., 2009).

2. ANALYTICAL METHODS

The splitting of the Fermi diad in the Raman spectrum of CO_2 was calibrated as a function of pressure and temperature using a high-pressure optical cell in the Vibrational Spectroscopy Laboratory in the Department of Geosciences at Virginia Tech. The experimental setup used for the calibration is similar to that used in a previous study to determine the pressure and temperature dependence of the position of the v_1 symmetric stretching band for methane that is located at approximately 2915 cm^{-1} (Lin et al., 2007). Kawakami et al. (2003) and Yamamoto and Kagi (2006) describe a similar experimental technique to determine CO_2 density, and Song et al. (2009) measured the Raman spectrum of CO_2 in fused silica capillaries to determine the relationship between peak splitting and density. The optical cell was connected to a manual screw press-type pressure generator (High-Pressure Equipment Model #50-6-15) and pressure was monitored using a Precise Instruments pressure transducer (Model 645) accurate to ±0.1% of the pressure output. Ultra-high purity CO_2 was used for calibration and the system was purged several times before each experiment to remove any other gases and/or water from the cell. The positions of the Fermi diad peaks were measured in 1.0 MPa increments in the 1–7 MPa range, and in 5 MPa increments in the 10–30 MPa range, at temperatures of −10°, −5°, 0°, 5°, 10°, 15°, 20°, and 22 °C. The Fermi diad peak splitting was also measured above the critical temperature of CO_2 (31.1 °C) at 35 °C with pressure increments of 0.5 MPa in the 1–6.5 MPa and 8.5–10.0 MPa ranges, 0.1 MPa increments in the 6.5–8.5 MPa range, and 2.5 MPa increments in the 10–30 MPa range. These data are available as an Electronic annex to this paper. The mean value of two measurements, recorded during increasing and decreasing pressure cycles, was taken as the Raman peak position at each pressure, although the difference between the two measurements was generally less than ±0.03 cm^{-1} (Electronic annex). The pressure cell was immersed in a liquid (50% pre-diluted Prestone® antifreeze coolant) bath to maintain a constant temperature during each analysis. An Omega type-E thermocouple, calibrated against the freezing point of H_2O at 0 °C, was inserted into a small hole drilled into the top of the pressure cell, 10 mm deep and 5 mm laterally from the gas chamber, to monitor the temperature. The accuracy of temperature measurements was estimated to be ±0.05 °C, and the temperature varied by <±0.05 °C during an individual Raman analysis.

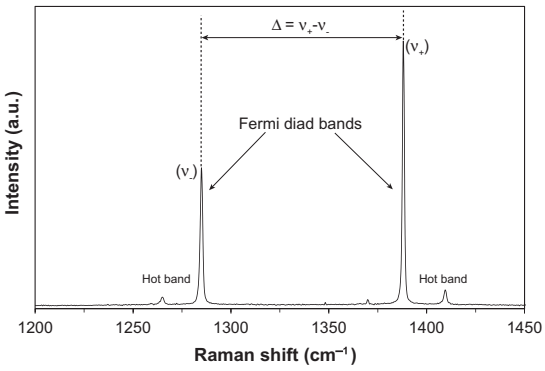

Fig. 3. Representative Raman spectrum showing the Fermi diad for CO_2. Δ represents the difference between the positions of the v_+ and v_- peaks of the Fermi diad, and the peak splitting is density (pressure) dependent. The low intensity hot bands are due to the thermal energy of the vibrating molecules and are not used in this study.

Raman analyses were performed using a JY Horiba LabRam HR (800 mm) spectrometer, with 600 grooves/mm and 2400 grooves/mm gratings. The 600 grooves/mm gratings were used during the initial stages of this study to obtain the calibration data. We subsequently acquired 2400 grooves/mm gratings for our instrument, and this setup was used for later fluid inclusion analyses. Comparison of results obtained from the 600 and 2400 groove gratings in our lab (Ferrero et al., 2010) showed insignificant differences in peak positions (after peak fitting) using the different analytical conditions. The slit width was set to 150 μm, and the confocal aperture at 400 μm. Excitation was provided by a 514.529 nm (green) Laser Physics 100S-514 Ar^+ laser. The laser output was 50 mW at the source and <10 mW at the sample. The laser was focused through a 3.5 × objective (N.A. = 0.10) with a working

distance of ~12 mm for the pressure cell. A 40× (N.A. = 0.55) objective with cover-glass correction to improve signal/background ratio (Adar et al., 2004) was used for fluid inclusion analyses. The beam diameter for the 40× objective was approximately 1 μm; the beam diameter for the 3.5× objective was not determined but is estimated to be on the order of 3–5 μm. The detector was an electronically cooled open electrode 1024 pixel CCD. Two accumulations of 10 s were used for pressure cell measurements, while the accumulation time for the fluid inclusions varied from 10 s to 3 min, optimized to achieve approximately similar peak intensities (counts) for fluid inclusions of different size, shape and depth beneath the surface.

The position of each measured Raman line was determined after baseline correction using Gaussian/Lorentzian peak fitting. Previous studies (Izraeli et al., 1999; Fukura et al., 2006) demonstrated that least-square fitting applied to Raman spectra improves the precision by ~30 times compared to that estimated based on the detector pixel resolution. However, the difference in peak position (splitting) for two peaks separated by a small range in wavenumbers is expected to be essentially independent of the absolute peak positions (McCreery, 2000). In this study it is the difference in peak positions, and not their absolute positions, that is important.

To confirm that the pressure at the clathrate melting temperature could be determined based on the splitting of the Fermi diad for CO_2 and then used along with P–T–X data to determine the salinity of the aqueous phase in the inclusion, we prepared synthetic fluid inclusions of known salinity using techniques described by Sterner and Bodnar (1984, 1991) and Azbej et al. (2007). Aqueous H_2O–NaCl solutions containing 5, 10, and 20 wt% NaCl were prepared. Pre-fractured, inclusion free, 15–20 mm long "Brazilian" quartz prisms, together with 100 μl of aqueous solution and a known amount of oxalic acid dihydrate ($C_2H_2O_4{\cdot}2H_2O$) were loaded into 25 mm long and 5 mm diameter platinum capsules and sealed by arc welding. The capsules were loaded into externally-heated cold seal pressure vessels, pressurized and heated to the desired experimental conditions of 150–160 MPa and 400–700 °C. During heating, the oxalic acid decomposes explosively at 157 °C to produce equimolal proportions of CO_2 and H_2O, as well as H_2, which diffuses out of the capsules at elevated temperatures (Mavrogenes and Bodnar, 1994). During the experiment the fractures heal and trap microdroplets of fluid in the process to produce fluid inclusions. As the masses of the components loaded into the capsules were known, the salinity of the bulk fluid in each capsule could be calculated. Note that the final (bulk) salinity of the inclusions was less than the salinity of the aqueous phase originally loaded into the capsules because the salinity was diluted by H_2O generated by the decomposition of the oxalic acid. The calculated salinities were 0.0, 3.1, 6.0, 8.1 and 11.1 wt% NaCl (relative to $H_2O + NaCl$). The experiments lasted 7–10 days, after which the pressure vessels were removed from the furnace and quenched in air. The platinum capsules were removed from the pressure vessels, cleaned and weighed to check for possible fluid loss during the experiment. Any capsules showing evidence of fluid loss were discarded. The quartz prisms were removed from capsules that showed no evidence of fluid loss during the experiment, sliced into 1 mm thick chips and polished on both sides in preparation for microthermometric analysis. In addition to the samples prepared in the present study, two samples with salinities of 20 and 40 wt% from an earlier study (Schmidt and Bodnar, 2000) were also analyzed.

Microthermometry was carried out on a Linkam THMSG 600 heating/freezing stage that was calibrated using the melting temperature of solid CO_2 at −56.6 °C in H_2O–CO_2 synthetic fluid inclusions, and the pure H_2O ice-melting temperature at 0 °C and the critical homogenization temperature at 374.1 °C, both measured in synthetic pure H_2O inclusions (Sterner and Bodnar, 1984). This same heating/cooling stage was later mounted onto the Raman microprobe to measure the positions of the Fermi diad peaks for CO_2 in fluid inclusions at the clathrate melting temperature.

3. RESULTS AND DISCUSSION

The relationship between CO_2 density and the distance between the peaks of the Fermi diad for CO_2 was determined over the range −10° to +35 °C and from 1 to 30 MPa. As shown on Fig. 4a, splitting of the Fermi diad is greater for the higher-density liquid phase than for the lower-density CO_2 vapor. Moreover, at a given pressure, temperature has little effect on the splitting for the CO_2 vapor, but a more pronounced temperature effect on the splitting is observed for the liquid CO_2 (Fig. 4a). This behavior is expected based on the slopes of the isochores in the CO_2 vapor field, compared to those in the CO_2 liquid field (see, for example, Fig. 1.1 in Hollister, 1981 or Fig. 5-1d in Diamond, 2003). That is, because the isochore slopes ($\Delta P/\Delta T$) are "shallow" in the vapor field, i.e., the isochores are "flat", changing the temperature at constant pressure results in a relatively small change in density. Conversely, because the isochores in the liquid field are "steep", a relatively small change in temperature at constant pressure results in a relatively large change in density.

The density of CO_2 in the pressure cell at a given temperature and pressure was calculated using the equation of state (EOS) for CO_2 of Span and Wagner (1996) in Lemmon et al. (2010). Densities obtained from the Span and Wagner (1996) EOS are plotted as a function of the splitting of the Fermi diad for CO_2 in Fig. 4b. With increasing pressure, both peaks of the Fermi diad move to lower wavenumbers and the distance between the peaks increases. With the exception of the 35 °C calibration run, all measurements were below the CO_2 critical temperature (31.1 °C). As a result, as the pressure in the cell was increased by turning the screw press, the density of CO_2 in the cell would increase until the pressure on the liquid–vapor curve was reached. At this point, liquid CO_2 would begin to condense as the volume of the system was decreased further by continued turning of the screw press, and the cell contained both vapor and liquid CO_2. As long as the cell contained both vapor and liquid CO_2 the pressure in the cell remained constant at the pressure on the liquid–vapor

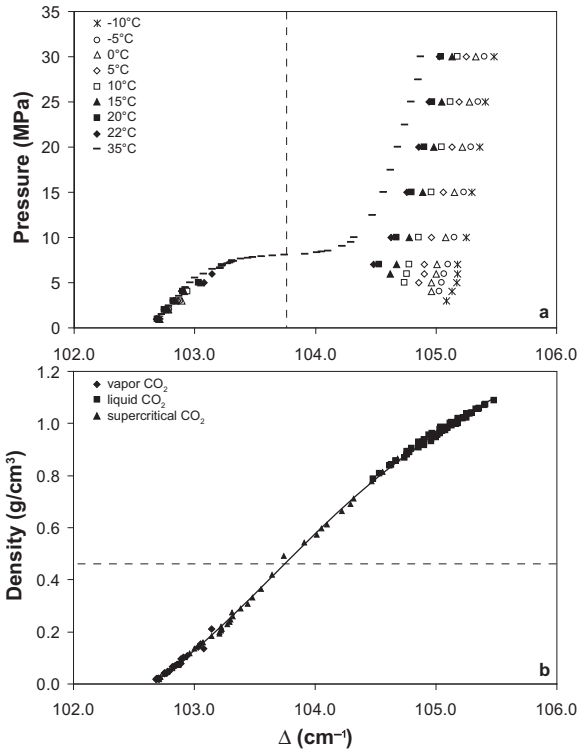

Fig. 4. (a) Relationship between the experimental pressure during calibration and the splitting of the Fermi diad for CO_2 measured in the high-pressure optical cell at various temperatures from −10 to +35 °C. The vertical dashed line at 103.77 cm^{-1} corresponds to the peak splitting for the critical density of CO_2 of 0.468 g/cm^3. (b) Density of CO_2 as a function of the distance between the v_+ and v_- peaks of the Fermi diad for CO_2 (Δ) measured in the high-pressure optical cell. The horizontal dashed line at 0.468 g/cm^3 corresponds to the critical density of CO_2. The fitted line in (b) was determined from Eq. (1), $\rho CO_2 = -0.030341551 \times \Delta^3 + 9.432834797 \times \Delta^2 - 977.9384933 \times \Delta + 33780.38242$, where ρCO_2 is the density of CO_2 in g/cm^3.

curve at that temperature. No Raman data were collected for densities of CO_2 vapor and the coexisting CO_2 liquid on the liquid–vapor curve, resulting in a gap in the density versus peak splitting for those temperatures. The gap in densities surveyed is evidenced by the two distinctive groupings of data on Fig. 4b.

Regression analysis of the calibration data produced the following 3rd order polynomial equation that relates CO_2 density to the splitting of the Fermi diad for CO_2:

$$\rho CO_2 = -0.030314551 \times \Delta^3 + 9.432834797 \times \Delta^2 - 977.9384933 \times \Delta + 33780.38242 \quad (1)$$

where ρCO_2 is the density of carbon dioxide in g/cm^3, and Δ is the distance between the two peaks of the Fermi diad in cm^{-1} (Fig. 3). Eq. (1) is similar in form (3rd order polynomial) and the coefficients are of the same order of magnitude as the equations of Kawakami et al. (2003) and Song et al. (2009). Yamamoto and Kagi (2006) present a 3rd order polynomial equation as well as an 8th order polynomial equation relating density and peak splitting. None of these earlier studies systematically examined the effect of temperature on the relationship between density and peak splitting. Kawakami et al. (2003) measured the peak splitting at 16.1–18.3 °C and at 57.4–58.4 °C, and Yamamoto and Kagi (2006) measured the peak splitting at 22.1–23.5 °C. Song et al. (2009) measured the peak splitting from −23.7 °C to 30.8 °C, but only along the CO_2 liquid–vapor curve. Densities predicted by Eq. (1) are compared to densities predicted by the models of Kawakami et al. (2003), Yamamoto and Kagi (2006) and Song et al. (2009) in Table 1.

To test the validity of the calibration data and Eq. (1), densities of both liquid and vapor CO_2 within the same inclusion were determined from the Fermi diad peak splitting and compared to the known densities of CO_2 on the liquid–vapor curve (Fig. 5). These tests also document the excellent spatial resolution of the Raman microprobe, as evidenced by the ability to focus the laser into either the liquid phase or the vapor CO_2 phase without interference from the other phase (Fig. 5a, inset). It should also be noted that the CO_2 phases did not homogenize during the analysis, indicating that heating of the inclusion during laser illumination is minimal. Previous experience in this laboratory suggests that CO_2-bearing inclusions are heated by no more than a few tenths of a degree during Raman analysis, based on the observation that inclusions in which the CO_2 homogenization temperature was only a few tenths of a degree above the ambient laboratory temperature did NOT homogenize when illuminated by the laser. Densities of the coexisting liquid and vapor CO_2 phases in salt-free H_2O–CO_2 fluid inclusions, calculated from Raman Fermi diad splitting using Eq. (1), are shown in Fig. 5a. Pressures corresponding to densities obtained from the liquid CO_2 phase are identical (within analytical uncertainty) to pressures obtained from the vapor CO_2 phase within the same inclusion (Fig. 5b), indicating that the P–T conditions are on the CO_2 L–V curve (as is required based on the coexistence of liquid and vapor CO_2 in the same inclusion). Moreover, the calculated densities of liquid and vapor CO_2 from the same inclusion agree with known densities (and pressures) along the CO_2 L–V curve (Fig. 5a and b). We note that densities of CO_2 vapor (coexisting with liquid CO_2) predicted by the Fermi diad splitting in some inclusions indicate pressures somewhat below the liquid–vapor curve at the temperature of the analysis, i.e., in the CO_2 vapor field. This results in an error of up to ±0.2 MPa in pressure determinations based on the density of the vapor phase.

Results described above document that the CO_2 density (and pressure) within an individual fluid inclusion can be determined based on the splitting of the Fermi diad peaks in the Raman spectrum of CO_2. This method was then applied to determine the salinity of fluid inclusions based on the temperature and pressure of clathrate melting. Eq. (1) was used to determine the density of CO_2 at the moment of clathrate melting in synthetic fluid inclusions containing H_2O–CO_2 ± NaCl solutions of various salinities. The fluid inclusions were cooled, using a heating/freezing stage that was mounted on the Raman microprobe, until a clathrate phase nucleated (Fig. 1). The clathrate always nucleates at the interface between one of the CO_2 phases (either liquid or vapor) and the liquid H_2O phase. During cooling from

Table 1
Comparison of results of this study with previously published data. All calculations at 20 °C.

1	2	3	4	5	6	7	8	9	10	11	12	13	14	15
Δ	ρ_1	P_1	ρ_2	$\rho\%_{1-2}$	P_2	$P\%_{1-2}$	ρ_3	ρ_{1-3}	P_3	$P\%_{1-3}$	ρ_4	ρ_{1-4}	P_4	$P\%_{1-4}$
102.7	0.019	1.0	0.103	−440	4.2	−317	0.077	−306	3.4	−239	0.008	59	0.4	56
103.0	0.134	4.9	0.213	−59	5.7	−18	0.204	−53	5.7	−18	0.134	0	4.9	0
104.0	0.573	5.7	0.650	−13	5.7	0	0.643	−12	5.7	0	0.571	0	5.7	0
105.0	0.962	24.8	1.046	−9	49.1	−98	1.018	−6	39.4	−59	0.972	−1	27.0	−9
105.5	1.081	64.0	1.168	−8	117.7	−84	1.146	−6	101.5	−59	1.132	−5	92.2	−44

1. CO_2 Fermi diad peak splitting (cm^{-1}).
2. CO_2 density (g/cm^3) determined using Eq. (1) (this study).
3. CO_2 pressure (MPa) corresponding to ρ_1 (this study).
4. CO_2 density (g/cm^3) determined using the equation of Kawakami et al. (2003).
5. Percent difference between density predicted in this study and that predicted by Kawakami et al. (2003).
6. CO_2 pressure (MPa) corresponding to density predicted by Kawakami et al. (2003).
7. Percent difference between pressure predicted in this study and that predicted by Kawakami et al. (2003).
8. CO_2 density (g/cm^3) determined using the equation of Yamamoto and Kagi (2006).
9. Percent difference between density predicted in this study and that predicted by Yamamoto and Kagi (2006).
10. CO_2 pressure (MPa) corresponding to density predicted by Yamamoto and Kagi (2006).
11. Percent difference between pressure predicted in this study and that predicted by Yamamoto and Kagi (2006).
12. CO_2 density (g/cm^3) determined using the equation of Song et al. (2009).
13. Percent difference between density predicted in this study and that predicted by Song et al. (2009).
14. CO_2 pressure (MPa) corresponding to density predicted by Song et al. (2009).
15. Percent difference between pressure predicted in this study and that predicted by Song et al. (2009).

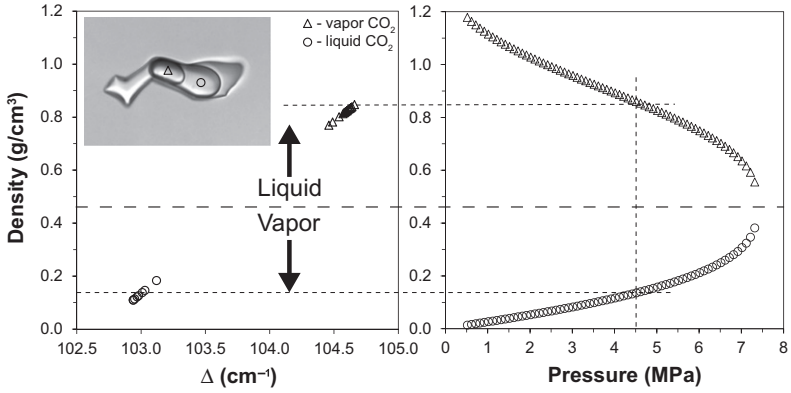

Fig. 5. (a) Density of CO_2 (from Lemmon et al., 2010) as a function of splitting of the Fermi diad (Δ) for the CO_2 vapor and liquid phases in synthetic fluid inclusions. (b) CO_2 density as a function of pressure along the L–V coexistence curve from Lemmon et al. (2010). Densities obtained from the coexisting CO_2 liquid and vapor phases in inclusions predict the same pressure along the CO_2 L–V curve as expected, in most cases. The thick horizontal dashed line at 0.468 g/cm^3 corresponds to the critical density of CO_2 that separates liquid from vapor.

room temperature, the aqueous phase remains metastable to about −30 °C, at which point clathrate and ice nucleate simultaneously. After clathrate and ice formed, the inclusion was heated at a controlled rate until the clathrate completely melted. Clathrate can melt in the presence of both liquid and vapor CO_2 (Fig. 1a–c), in the presence of CO_2 vapor only (Fig. 1d–f), or in the presence of liquid CO_2 only (Fig. 1g–i). Clathrate dissociation (melting) is sluggish, much like that reported for dissociation of hydrohalite by Roedder (1963), and special care had to be taken to determine the equilibrium melting temperature. The analytical protocol used to measure the clathrate melting temperature is similar to the technique that has been used in our lab (and in many other fluid inclusions labs) to determine clathrate melting temperatures in natural and synthetic fluid inclusions. First, after clathrate (and ice ± hydrohalite) formed, a heating rate of ≈5 °C/min was used to heat the inclusion to a temperature close to the clathrate melting temperature. Then, a thermal cycling technique (Goldstein and Reynolds, 1994) was used to determine the clathrate melting temperature. The inclusions were heated at a slower rate (≈0.5 to 1.0 °C/min) until the clathrate phase was no longer visible in the fluid inclusion, and then the temperature was held constant for up to several minutes. Then, the inclusions were continuously monitored as they were quickly cooled by several degrees. If clathrate was still present in the inclusion (even though it was not recognizable optically), the clathrate phase would begin to grow at the CO_2 phase – aqueous phase interface with a small temperature decrease. It should be noted that the temperature at which the clathrate was observed to grow during thermal cycling was several tens of degrees higher than the

temperature at which clathrate nucleated originally when the inclusion was cooled from room temperature. Once the presence of clathrate was confirmed in this way, the inclusion was heated again to a temperature 0.1 °C higher than the previous maximum temperature, and the process was repeated until the clathrate was no longer observed to immediately grow back during subsequent cooling. In most cases, after the clathrate melting temperature was determined as described above, one more cooling experiment was conducted in which the clathrate-free inclusion was cooled from room temperature to low temperature to again nucleate clathrate. The inclusion was then heated to a temperature 0.1 °C *below* the temperature previously determined as the equilibrium clathrate melting temperature. The inclusion was held at this temperature for a longer period of time, sometimes up to 30 min, and then cooled to confirm that the clathrate did indeed grow back. This test confirmed that the previously determined clathrate melting temperature was not a result of metastability and that the inclusion had been held at temperature during the previous run for a sufficient length of time to achieve equilibrium melting. In most cases, the clathrate grew back when held for longer times at a temperature 0.1 °C lower than the previously determined clathrate melting temperature, confirming that the previously measured temperature represents the equilibrium melting temperature. In a few cases the clathrate did not grow back after being held for a longer time at a temperature 0.1 °C below the presumed equilibrium melting temperature. In these cases, the temperature at which the inclusion was held was lowered by 0.1 °C and held at this new temperature for several tens of minutes, and then cooled rapidly. In every case, the clathrate did not grow back after the temperature was decreased from the original value by 0.1 °C, indicating that the clathrate melting temperature determination had a precision (and accuracy) of ±0.05 °C.

As noted above, the goal of this study was to use the splitting of the Fermi diad peak for CO_2, measured at the temperature at which clathrate melts during heating, to determine the pressure at clathrate melting and to use this information, in turn, to determine the salinity of the fluid inclusion. And, as described above, determining the clathrate melting temperature accurately is a tedious and time-consuming process. During the course of this work numerous Raman analyses of synthetic inclusions were conducted at the temperature at which the clathrate phase melted during slow heating and temperature cycling as described above, and the density (and pressure) in the inclusions at this temperature was determined from the Fermi diad peak splitting. However, after we had determined the clathrate melting temperature for an inclusion, we analyzed many of these same inclusions after they were cooled from room temperature to the previously determined clathrate melting temperature, but *without* nucleating clathrate in the inclusions. In all inclusions studied, we found excellent agreement between Fermi diad splitting (and the density of CO_2) obtained when the inclusions were analyzed during the heating cycle (and immediately following clathrate melting) and Fermi diad splitting obtained during simple cooling to the previously determined clathrate melting temperature (Fig. 6).

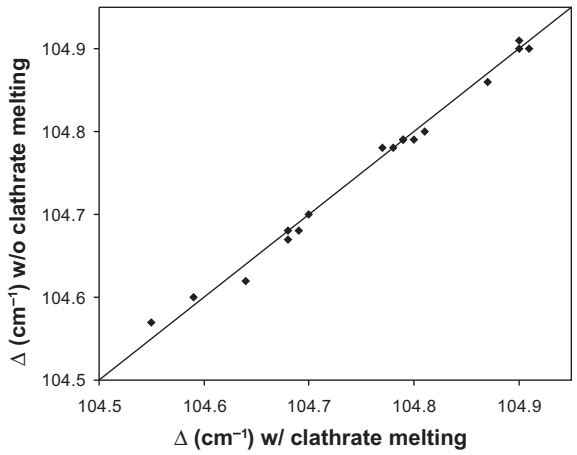

Fig. 6. Splitting of the Fermi diad for CO_2 at the clathrate melting temperature determined during heating from low temperature and using thermal cycling (ordinate) technique versus splitting of the Fermi diad in the same inclusion after cooling the clathrate-free inclusion to the previously determined clathrate melting temperature (abscissa), but without nucleating clathrate.

At the ternary peritectic in the H_2O–CO_2–NaCl system (Fig. 7), five phases coexist in equilibrium: clathrate, hydrohalite ($NaCl{\cdot}2H_2O$), liquid CO_2, vapor CO_2 and an aqueous phase with a salinity of 24.2 wt% NaCl (Chen, 1972; Bozzo et al., 1973, 1975; Barton and Chou, 1993). The pressure at this quintuple point was determined in this study using H_2O–CO_2–NaCl synthetic fluid inclusions with a salinity of 40 wt% NaCl (relative to H_2O + NaCl). Note that in these inclusions clathrate melts at the quintuple point to produce an assemblage consisting of liquid CO_2, vapor CO_2, hydrohalite, and an aqueous phase, and the hydrohalite phase melts at a second peritectic at higher temperature (≈0.1 °C; Barton and Chou, 1993) where the five phases liquid CO_2, vapor CO_2, hydrohalite, halite and an aqueous phase coexist. Thus, hydrohalite melts at a temperature above the temperature of clathrate melting. To avoid interference from the hydrohalite phase during collection of the Raman spectrum of CO_2, the inclusions were heated until hydrohalite melted, after which the inclusions were cooled to the observed clathrate melting temperature. The Fermi diad splitting of the CO_2 peaks was measured at the previously determined clathrate melting temperature without allowing clathrate or hydrohalite to nucleate, i.e., the inclusions were not super-cooled to initiate "freezing". Note that although the equilibrium phase assemblage was not present when these inclusions were analyzed at the ternary peritectic, the pressure was equal to the equilibrium pressure at the quintuple point because both liquid and vapor CO_2 were present, requiring that the P–T conditions are on the CO_2 liquid–vapor curve.

After the clathrate dissociation temperature was determined, the sample was maintained at that temperature (±0.05 °C) and the Raman spectrum was collected. Between 8 and 10 inclusions were measured within each sample. If the inclusions contained both liquid and vapor CO_2 at the temperature of clathrate melting, a Raman spectrum was collected from each phase, taking advantage of the

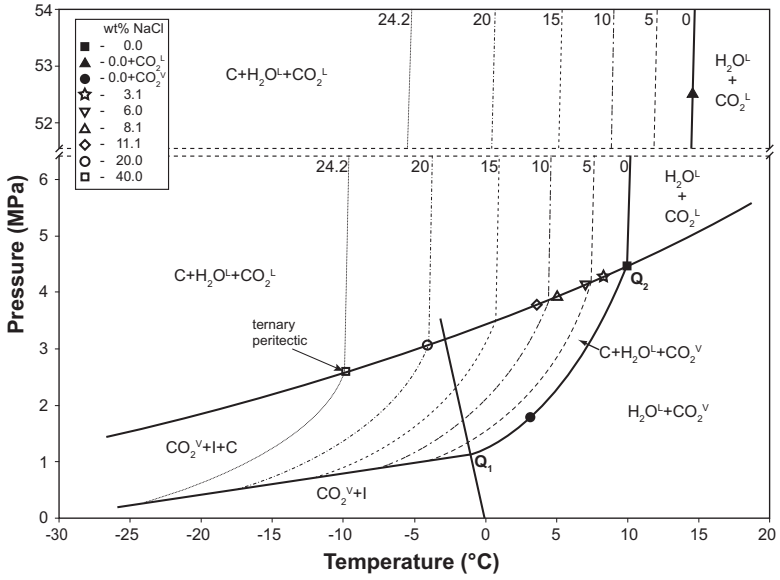

Fig. 7. Low temperature phase equilibria in the system H_2O–CO_2–NaCl. The data points represent pressures determined from Raman spectroscopic analysis at the clathrate melting temperatures for synthetic fluid inclusions of various salinities. Solid lines represent phase boundaries for pure CO_2 and for H_2O–CO_2 based on experimental data of Larson (1955). Dashed lines represent clathrate stability curves for various salinities labeled in wt% NaCl based on the computer program package "Clathrates" of Bakker (1997) and Bakker and Brown (2003). Abbreviations are the same as in Fig. 2.

excellent spatial resolution of the Raman microprobe. Using Eq. (1), the density of the CO_2 phase(s) at the clathrate melting temperature was determined for individual fluid inclusions. Knowing the density of the CO_2 phase(s) at the clathrate melting temperature permitted calculation of the pressure within the inclusion using the equation of state for CO_2 of Span and Wagner (1996) in Lemmon et al. (2010). Fig. 7 shows results obtained in this study. Heavy solid lines on Fig. 7 represent the CO_2 liquid–vapor curve and CO_2 clathrate P–T stability limits in the H_2O–CO_2 system (line labeled '0' on Fig. 7) based on experimental data of Larson (1955). The dashed and dashed-dot lines show the P–T stability limits for clathrate in equilibrium with aqueous solutions of various salinities, estimated using the computer program package "Clathrates" of Bakker (1997) and Bakker and Brown (2003). Also shown by the lighter solid line labeled "24.2" is the melting curve for clathrate in equilibrium with a solution having the eutectic salinity (24.2 wt% NaCl).

For most of the samples studied, the clathrate phase in the inclusions melted in the presence of both liquid and vapor CO_2 (Table 2 and Fig. 7). For these inclusions, the pressure in the inclusion at the clathrate melting temperature equals the pressure on the CO_2 liquid–vapor curve. Pressures determined from the splitting of the Fermi diad of CO_2 in this study were compared with pressures on the CO_2 liquid–vapor curve (Lemmon et al., 2010), and with pressures for clathrate melting predicted by published models (Bakker, 1997; Sun and Duan, 2005) (Table 2). There is excellent agreement between the pressures determined in this study from the Fermi diad splitting and those predicted by the various models described above, except for the sample that shows melting at the ternary peritectic point (40 wt% NaCl sample), where the model of Sun and Duan (2005) predicts a pressure significantly lower than that determined in this study and predicted by Bakker (1997)

Table 2
Pressures at the clathrate melting temperature determined in this study compared with values from the literature.

1	2	3	4	5	6
S	*T*	P_1	P_2	P_3	P_4
0.0[a]	10.0	4.5	4.5	4.5	4.5
0.0[b]	14.8	52.4 (10[d], 50–55[e])	–	66.1	–
0.0[c]	2.8	1.9 (9[d], 1.7–2.2[e])	–	1.7	–
3.1	8.6	4.3	4.3	4.4	4.4
6.0	7.3	4.2	4.2	4.3	4.2
8.1	5.6	4.0	4.0	3.8	4.0
11.1	3.6	3.8	3.8	3.4	3.8
20.0	−4.4	3.0	3.1	2.0	3.1
40.0	−9.9	2.7	2.7	1.3[f]	2.7

1. Salinity of the aqueous phase (wt% NaCl) at the temperature of clathrate melting.
2. Clathrate melting temperature (°C).
3. Pressure (MPa) at the clathrate melting determined by Raman spectroscopy in this study.
4. Pressure (MPa) on the CO_2 liquid–vapor curve at the clathrate melting *T* (Lemmon et al., 2010).
5. Pressures (MPa) at clathrate melting predicted by the equation of state of Sun and Duan (2005).
6. Pressures (MPa) at clathrate melting predicted by the 'Q_2' software of Bakker (1997).

[a] Clathrate melting at the Q_2 point shown on Figs. 2 and 7 in presence of both liquid and vapor CO_2.
[b] Clathrate melting in the presence of liquid CO_2 only.
[c] Clathrate melting in the presence of vapor CO_2 only.
[d] Number of synthetic fluid inclusions analyzed.
[e] Range of pressures (MPa) at clathrate melting.
[f] Pressure calculated at the ternary peritectic (24.2 wt% NaCl).

and Lemmon et al. (2010). The generally good agreement suggests that the combined Raman-microthermometry technique can be used to estimate pressures in H_2O–CO_2–NaCl fluid inclusions at the temperature of clathrate melting and that this pressure, in turn, can be interpreted based on experimental data and numerical models to predict the salinity of the inclusion.

If the clathrate phase melts in the presence of both CO_2 liquid and vapor, then the Raman technique described here is not required to determine the pressure at the clathrate melting temperature, because the pressure at clathrate melting equals the pressure on the CO_2 liquid–vapor curve and can be obtained from the EOS for CO_2, as described above. However, when the clathrate phase melts in the presence of only CO_2 liquid or only CO_2 vapor, the pressure cannot be determined from microthermometric data or from an EOS directly. Using the algorithms of Connolly and Bodnar (1983) and Bodnar et al. (1985b), it is possible to predict the range in P–T–X trapping conditions that will result in clathrate melting in the absence of coexisting liquid and vapor CO_2. For example, Fig. 8 shows the combination of pressure – mole percent CO_2 values at 500 °C that will produce fluid inclusions that show CO_2 liquid–vapor homogenization temperatures of $<+10$ and <-10 °C. As shown on Fig. 8, any pressure – mole percent CO_2 trapping condition at 500 °C that falls within the shaded regions will result in fluid inclusions that show clathrate melting in the presence of both liquid and vapor CO_2. Any inclusions trapped outside of the shaded regions will show clathrate melting in the presence of CO_2 liquid only (high pressures) or CO_2 vapor only (low pressures). Thus, those inclusions trapped at 500 °C and which have relatively high CO_2 contents and are trapped at relatively high pressures will NOT show clathrate melting in the presence of both liquid CO_2 and vapor CO_2 (the clathrate will melt in the presence of liquid CO_2 only). Similarly, inclusions trapped at very low pressures and having low CO_2 contents will show clathrate melting in the presence of CO_2 vapor only. Thus, the combined Raman spectroscopy-microthermometry technique described here could be used to determine the salinities of fluid inclusions trapped at these extreme ranges of pressure and CO_2 content, and might include CO_2-rich inclusions from high pressure environments such as granulite terrains (Touret, 1981, 2001) or the upper mantle (Berkesi et al., 2009), or from high temperature, low pressure volcanic environments (Roedder, 1984).

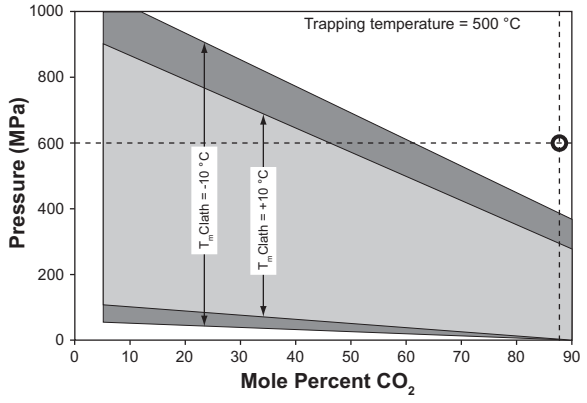

Fig. 8. Calculated ranges in trapping pressure and fluid composition at 500 °C that will result in fluid inclusions in which the CO_2 phases homogenize at +10 °C or higher (light shaded region) and at −10 °C or higher (dark shaded region). Inclusions trapped at 500 °C and at pressure – composition conditions outside of the shaded regions will show CO_2 homogenization temperatures less than −10 °C (dark shaded region) or less than +10 °C (light shaded region). Data were calculated using the models of Connolly and Bodnar (1983) and Bodnar et al. (1985b), which are mass balance models based on P–V–T–X data for the system H_2O–CO_2. The circle at 600 MPa and 87.5 mol% CO_2 corresponds to the formation conditions for the inclusion listed in Table 2 and shown on Fig. 7 that showed clathrate melting in the presence of liquid CO_2 only (plus liquid H_2O) at 14.8 °C and 52.4 MPa.

Two samples in this study contained H_2O–CO_2 synthetic fluid inclusions that did not show clathrate melting in the presence of both liquid and vapor CO_2. One showed clathrate melting in the presence of liquid CO_2 only (Fig. 7 and Table 2), and the other showed melting in the presence of CO_2 vapor only (Fig. 7 and Table 2). Pressures determined in this study for the inclusions in which melting occurred in the presence of CO_2 vapor only agree reasonably well with pressures predicted by the EOS of Sun and Duan (2005) (Table 2). However, the pressure determined in this study for the inclusions that showed clathrate melting in the presence of only liquid CO_2 is 52.4 ± 2.5 MPa, which is significantly lower than the 66.1 MPa predicted by Sun and Duan (2005) (Table 2). One possible explanation for the discrepancy is that the slope of the clathrate phase boundary in the liquid CO_2 region is very steep (Fig. 7), and, therefore, a small error in temperature results in a large error in pressure.

4. ERROR ANALYSIS

The error in salinity is a function of the error in measured splitting of the Fermi diad for CO_2 which, in turn, affects the calculated CO_2 density and pressure. While the position of a single peak may vary significantly from one measurement to the next, the difference in peak positions varies much less. For example, in a study of the relationship between pressure and the position of the Raman peak for methane Lin et al. (2007) measured the positions of two Ne peaks that closely-bounded the methane peak. A total of 231 analyses of the peak positions were made, and the measured position of the higher wavenumber Ne line varied from 2972.91 to 2972.44 cm^{-1}, or a range of 0.47 cm^{-1}. Similarly, the measured position of the lower wavenumber Ne line ranged from 2851.86 to 2851.40 cm^{-1}, for a total variation of 0.46 cm^{-1}. However, the *difference* in peak positions showed a range of only 0.05 cm^{-1}, with standard deviation of 0.012 cm^{-1}. Thus, while the measured positions of the individual peaks varied by several tenths of a wavenumber, the difference in peak positions was an order of magnitude less.

In this study, the Fermi diad splitting for CO_2 was measured twice at each temperature and pressure during calibration, one measurement obtained during an increasing pressure cycle, and the other during a decreasing pressure cycle (Electronic annex). For each pair of peak splitting

measurements, the difference in peak splitting between the increasing pressure measurement and the decreasing pressure measurement was calculated. Then, the standard deviation for all such measurements at a given temperature was determined and, finally, the average standard deviation for all temperatures was calculated. The standard deviation for a given temperature ranged from 0.005 cm^{-1} at 10 °C to 0.045 cm^{-1} at 22 °C, and the average standard deviation for all temperatures from −10 to 22 °C (96 pairs of Fermi diad splitting measurements) was 0.013 cm^{-1} (1σ).

The second component of the error in peak splitting is related to how well Eq. (1) reproduces the measured values. The R^2 value for Eq. (1) is 0.9996 and the standard error is 0.022 cm^{-1}. The sum of the error in peak splitting from the calibration data (0.013 cm^{-1}) and that from Eq. (1) (0.022 cm^{-1}) is ±0.035 cm^{-1}, and represents the total error in peak splitting.

The error in density corresponding to the error in peak splitting was estimated using Eq. (1). Because the relationship between peak splitting and density is not linear, the density errors corresponding to the smallest peak splitting listed in Table 1 (102.7 cm^{-1}) and to the largest peak splitting in Table 1 (105.5 cm^{-1}) were calculated assuming an error in peak splitting of ±0.035 cm^{-1}. For the smaller peak splitting (102.7 ± 0.035 cm^{-1}) the density varies from 0.007 g/cm^3 (102.665 cm^{-1}) to 0.032 g/cm^3 (102.735 cm^{-1}), while for the larger peak splitting (105.5 ± 0.035 cm^{-1}) the density ranges from 1.075 (105.465 cm^{-1}) to 1.086 g/cm^3 (102.535 cm^{-1}). We note that the density error is not constant over the complete range of measured peak splitting (and density) determined here, as suggested by Yamamoto and Kagi (2006), because the relationship between pressure and CO_2 density is not linear.

The pressure errors associated with the errors in density described above may be estimated using an equation of state that relates temperature, pressure, and density of CO_2. In this study, we used the online NIST calculator for thermophysical properties of fluids (Lemmon et al., 2010). We note that over the P–T range of this study, differences in P–V–T properties for CO_2 predicted by the various EOS are negligible, and the NIST calculator was used owing to its flexibility and ease of use. As with the relationship between density and peak splitting described above, the relationship between density and pressure is not linear, and thus we have calculated the pressure error associated with the error in density for the low density example above as well as for the high density example. Moreover, because fluid isochores diverge or fan out with increasing temperature, the relationship between density and pressure also varies with temperature. We have estimated the error at both −10 °C and at 22 °C. At −10 °C, CO_2 has a density of 0.007 g/cm^3 at a pressure of 0.35 MPa, whereas at this same temperature CO_2 has a density of 0.032 g/cm^3 at a pressure of 1.45 MPa. Thus, the pressure error corresponding to the error in density reported above is ±0.55 MPa. At 22 °C, the pressure error for this same range in density is slightly larger at ±0.63 MPa. The corresponding errors for the higher density example are ±2.0 MPa at −10 °C, and ±2.6 MPa at 22 °C.

In order to estimate the error in salinity corresponding to the pressure error, we have selected intermediate values for the peak splitting and temperature to assure that the isotherm will intersect a range of salinities along the clathrate melting curve. At 0 °C, an error in the peak splitting of 0.035 cm^{-1} for a measured peak splitting of 102.84 cm^{-1} corresponds to a range in predicted density of from 0.058 to 0.084 g/cm^3. A nominal peak splitting of 105.70 cm^{-1} (±0.035 cm^{-1}) corresponds to a range in density of from 0.973 to 0.993 g/cm^3. These density ranges correspond to a range in pressure from 2.4 to 3.2 MPa (in the vapor field) and from 9.8 to 13.5 MPa (in the liquid field) respectively.

The error in salinity corresponding to the ranges in pressure reported above were estimated at 0 °C by entering various salinity values into the numerical model of Sun and Duan (2005) until a pressure equal to the pressures reported above were returned. Thus, according to Sun and Duan (2005), CO_2 clathrate melts at 0 °C and 2.4 MPa in equilibrium with a solution having a salinity of 2.35 m, or 12.1 wt% NaCl. At 0 °C and 3.2 MPa, the salinity predicted by Sun and Duan (2005) for a saline solution in equilibrium with CO_2 clathrate is 3.09 m, or 15.3 wt% NaCl. Thus, the error in salinity corresponding to the error in peak position for clathrate melting in the presence of CO_2 vapor only is 3.2 wt% NaCl at this condition, and the errors for other P–T conditions below the CO_2 liquid–vapor curve (i.e., clathrate melting in the presence of CO_2 vapor only) are expected to be of the same order of magnitude.

The salinity error for P–T conditions above the CO_2 liquid–vapor curve (clathrate melting in the presence of CO_2 liquid only) is expected to differ from that below the liquid–vapor curve (clathrate melting in the presence of CO_2 vapor only) because the relative pressure error is different for P–T conditions above the liquid–vapor curve as described above, and because the P–T slopes of the clathrate melting curves are steeper for clathrate melting in the presence of CO_2 liquid only (Fig. 7). As an example, the pressure range reported above for clathrate melting in the presence of CO_2 liquid only and corresponding to densities ranging from 0.973 to 0.993 g/cm^3 is 9.8 to 13.5 MPa. According to Sun and Duan (2005) clathrate melts at 0 °C and 9.8 MPa in equilibrium with an aqueous phase with a salinity of 3.57 m, or 17.3 wt% NaCl, and clathrate melts at 13.5 MPa in equilibrium with an aqueous phase with a salinity of 3.66 m, or 17.6 wt% NaCl. Thus, the error in salinity in this case is 0.3 wt% NaCl, or about an order of magnitude less than the salinity error for P–T conditions below the CO_2 liquid–vapor curve, i.e., where clathrate melts in the presence of CO_2 vapor only. Note that, owing to the differing slopes of the CO_2 isochores and the P–T slopes of the clathrate phase boundaries below and above the CO_2 liquid–vapor curve, even though the pressure error is significantly larger for clathrate melting in the presence of CO_2 liquid compared to melting in the presence of CO_2 vapor, the salinity error for clathrate melting above the CO_2 liquid–vapor curve is less than that for melting below the CO_2 liquid–vapor curve, i.e., in the presence of CO_2 vapor only.

5. OTHER APPLICATIONS

In this study, the relationship between splitting of the peaks of the Fermi diad in the Raman spectrum of CO_2

was used to determine the density in a fluid inclusion at the moment of clathrate melting, and this information, in turn, was used to determine the pressure at clathrate melting and, finally, the salinity of the aqueous phase in the inclusion. As such, the method described here has other potential applications in fluid inclusion and clathrate research.

Recently, Lin et al. (2007) determined the relationship between the position of the Raman symmetric stretching mode (v_1) for CH_4 as a function of temperature and pressure and then applied this relationship to determine the pressure in fluid inclusions at the temperature of methane clathrate melting. These workers proposed that the technique could be used in clathrate research to determine the relationship between clathrate melting, temperature, pressure and salinity, and a similar approach could be used to study clathrate equilibria in the H_2O–CO_2–"salt" system using the splitting of the Fermi diad for CO_2 to determine the pressure in synthetic fluid inclusions at clathrate melting. Lin and Bodnar (2010) used the same relationship between peak position and pressure (or density) for CH_4, combined with mass balance constraints, to determine the P–V–T properties of H_2O–CH_4 fluids over a range of P–T–X conditions. This approach has been applied to natural fluid inclusions in the H_2O–CH_4–"salt" system to determine compositions and densities of fluids associated with hydrocarbon gas migration in sedimentary basins (Becker et al., 2010). The methodology developed here for the system H_2O–CO_2–NaCl could be applied, along with Raman techniques to determine the bulk H_2O/CO_2 ratio of individual fluid inclusions (c.f., Azbej et al., 2007), to determine the composition and P–V–T properties of fluid inclusions approximated by the system H_2O–CO_2–NaCl. Thus, the method described in this paper, combined with previously described techniques to determine H_2O/CO_2 ratios of individual fluid inclusions, may be used to determine bulk compositions (including salinity) of inclusions which may then be interpreted using published equations of state to calculate fluid isochores and to interpret P–T trapping conditions for the inclusions.

Today the synthetic fluid inclusion technique is used routinely to study various fluid properties at elevated P–T conditions (Sterner and Bodnar, 1984; Bodnar and Sterner, 1987), including systems involving silicate melt and aqueous fluids (Student and Bodnar, 1999). In a recent study of the effect of CO_2 on copper partitioning between silicate melts and magmatic fluids, Tattitch et al. (2010) trapped synthetic H_2O–CO_2–NaCl inclusions in the two-fluid phase field at 800 °C and 100 MPa. Clathrate in the vapor-rich inclusions melted in the presence of CO_2 vapor only at 4.5 °C, and the Fermi diad splitting for these inclusions was 102.82 cm^{-1}. According to Eq. (1), this peak splitting corresponds to a CO_2 density of 0.063 g/cm^3, which corresponds to a CO_2 pressure of 2.6 MPa at 4.5 °C. The model of Sun and Duan (2005) predicts a salinity of 0.75 m, or 4.2 wt% NaCl, for clathrate melting at 4.5 °C and 2.6 MPa. Because salinity (or more correctly, Cl content) is one of the most important factors controlling the metal transport capability of hydrothermal fluids, it is critical to be able to estimate the salinity of fluids trapped during experiments, and the technique described here provides a simple and straightforward method of obtaining the salinity of CO_2-bearing fluids.

6. SUMMARY

Fluid inclusions approximated by the system H_2O–CO_2–NaCl are common in many geologic environments and provide valuable information concerning the pressure, temperature and composition history of fluids present. A major limitation that has reduced our ability to use these inclusions to determine the P–T history of the host rocks has been our inability to accurately determine the salinity of the inclusions. Several models and equations based on experimental or theoretical data exist that relate final clathrate melting temperatures to salinity for inclusions in which clathrate melts in the presence of both liquid and vapor CO_2, but determining the salinity of inclusions in which clathrate melts in the presence of either CO_2 liquid *or* CO_2 vapor has been problematic. The proposed analytical technique combines data from Raman spectroscopy and fluid inclusion microthermometry to obtain pressure at the clathrate melting temperatures for individual fluid inclusions in which clathrate melts in the presence of only CO_2 liquid *or* only CO_2 vapor. Results obtained on synthetic fluid inclusions with known salinity are in good agreement with existing models and experimental data, suggesting that the proposed method may be used to estimate the salinity of H_2O–CO_2–NaCl fluid inclusions. The relative error in salinity is, however, greater for inclusions in which clathrate melts in the presence of only CO_2 vapor, compared to those in which clathrate melts in the presence of only CO_2 liquid.

ACKNOWLEDEGEMENTS

The authors thank Charles Farley for his help with experimental design and operation of the high-pressure optical cell, and Martin A. Ziemann for advice on Raman spectroscopic analyses. Cs. Szabó, J.D. Rimstidt, R.J. Tracy and R.P. Lowell reviewed an early draft of the manuscript and provided many useful suggestions. The authors also thank I-Ming Chou and two anonymous GCA reviewers for their many comments and suggestions that clarified the presentation and significantly improved the manuscript. This material is based upon work supported by the National Science Foundation under Grant No. EAR-0711333 to R.J.B. Work presented by B.T. is supported by the National Science Foundation under Grant Nos. EAR-0738992, EAR-0911098, and EAR-0842205 to Philip Candela and Philip Piccoli. A.F. publishes with the approval of the director of the Bureau of Economic Geology.

APPENDIX A. SUPPLEMENTARY DATA

Supplementary data associated with this article can be found, in the online version, at doi:10.1016/j.gca.2010.11.021.

REFERENCES

Adar F., Naudin C., Whitley A. and Bodnar R. J. (2004) Use of a microscope objective corrected for a cover glass to improve confocal spatial resolution inside a sample with finite index of refraction. *App. Spectr.* **58**, 1136–1137.

Azbej T., Severs M. J., Rusk B. G. and Bodnar R. J. (2007) In situ analysis of individual H_2O–CO_2 fluid inclusions by laser Raman spectroscopy. *Chem. Geol.* **237**, 255–263.

Bakker R. J. (1997) Clathrates: computer programs to calculate fluid inclusion V-X properties using clathrate melting temperatures. *Comput. Geosci.* **23**, 1–18.

Bakker R. J. and Brown P. E. (2003) Computer modeling in fluid inclusion research. In *Fluid Inclusions: Analysis and Interpretation* (eds. I. Samson, A. Anderson and D. Marshall). *Min. Assoc. Can. Short Course,* vol. 32. pp. 175–212.

Barton P. B. and Chou I. M. (1993) Refinement of the evaluation of the role of CO_2 in modifying estimates of the pressure of epithermal mineralization. *Econ. Geol.* **88**, 873–884.

Becker S. P., Eichhubl P., Laubach S. E., Reed R. M., Lander R. H. and Bodnar R. J. (2010) A 48 m.y. history of fracture opening, temperature, and fluid pressure: Cretaceous Travis peak Formation, East Texas basin. *GSA Bull.* **122**, 1081–1093.

Berkesi M., Hidas K., Guzmics T., Dubessy J., Bodnar R. J., Szabó Cs., Vajna B. and Tsunogae T. (2009) Detection of small amounts of H_2O in CO_2-rich fluid inclusions using Raman spectroscopy. *J. Raman Spectrosc.* **40**, 1461–1463.

Bodnar R. J. (1993) Revised equation and table for determining the freezing pint depression of H_2O–NaCl solutions. *Geochim. Cosmochim. Acta* **57**, 683–684.

Bodnar R. J. (1995) Fluid inclusion evidence for a magmatic source for metals in porphyry copper deposits. In *Magmas, Fluids and Ore Deposits* (ed. J. F. H. Thompson). *Min. Assoc. Can. Short Course*, vol. 23. pp. 139–152.

Bodnar R. J. (2003) Introduction to aqueous-electrolyte fluid inclusions. In *Fluid Inclusions: Analysis and Interpretation* (eds. I. Samson, A. Anderson and D. Marshall). *Min. Assoc. Can. Short Course*, vol. 32. pp. 81–100.

Bodnar R. J., Burnham C. W. and Sterner S. M. (1985a) Synthetic fluid inclusions in natural quartz. III. Determination of phase equilibrium properties in the system H_2O–NaCl to 1000 °C and 1500 bars. *Geochim. Cosmochim. Acta* **49**, 1861–1873.

Bodnar R. J., Reynolds T. J. and Kuehn C. A. (1985b) Fluid inclusion systematics in epithermal systems. In *Geology and Geochemistry of Epithermal Systems* (eds. B. R. Berger and P. M. Bethke). Rev. Econ. Geol., vol. 2. pp. 73–98.

Bodnar R. J. and Sterner S. M. (1987) Synthetic fluid inclusions. In *Hydrothermal Experimental Techniques* (eds. G. C. Ulmer and H. L. Barnes). Wiley-Interscience, New York, pp. 423–457.

Bozzo A. T., Chen H.-S., Kass J. R. and Barduhn A. J. (1973) The properties of the hydrates of chlorine and carbon dioxide. In *The Fourth International Symposium on Fresh Water from the Sea*, vol. 3 (eds. A. Delyannis and E. Delyannis). pp. 437–451.

Bozzo A. T., Chen H.-S., Kass J. R. and Barduhn A. J. (1975) The properties of the hydrates of chlorine and carbon dioxide. *Desalination* **16**, 303–320.

Chen H.-S. (1972) The thermodynamics and composition of carbon dioxide hydrate. MS thesis, Syracuse University, Syracuse, New York.

Collins P. L. F. (1979) Gas hydrates in CO_2-bearing fluid inclusions and the use of freezing data for estimation of salinity. *Econ. Geol.* **74**, 1435–1444.

Connolly J. A. and Bodnar R. J. (1983) A modified Redlich–Kwong equation of state for H_2O–CO_2 mixtures: application to fluid inclusion studies. *EOS* **64** (abstr.), 350.

Crawford M. L. (1981) Fluid inclusions in metamorphic rocks – low and medium grade. In *Fluid Inclusions: Applications to Petrology* (eds. L. S. Hollister and M. L. Crawford). *Min. Assoc. Can. Short Course*, vol. 6. pp. 157–181.

Darling R. S. (1991) An extended equation to calculate NaCl contents from final clathrate melting temperatures in H_2O–CO_2–NaCl fluid inclusions: implications for P–T isochore location. *Geochim. Cosmochim. Acta* **55**, 3869–3871.

Diamond L. W. (1992) Stability of CO_2 clathrate hydrate + CO_2 liquid + CO_2 vapour + aqueous KCl–NaCl solution: experimental determination and application to salinity estimates of fluid inclusions. *Geochim. Cosmochim. Acta* **56**, 273–280.

Diamond L. W. (1994) Salinity of multivolatile fluid inclusions determined from clathrate hydrate stability. *Geochim. Cosmochim. Acta* **58**, 19–41.

Diamond L. W. (2003) Introduction to gas-bearing, aqueous fluid inclusions. In *Fluid Inclusions: Analysis and Interpretation* (eds. I. Samson, A. Anderson and D. Marshall). *Min. Assoc. Can. Short Course*, vol. 32. pp. 101–158.

Dubessy J., Thiery R. and Canalis M. (1992) Modelling of phase equilibria involving mixed gas clathrates: application to the determination of molar volume of the vapour phase and salinity of the aqueous solution in fluid inclusions. *Eur. J. Mineral.* **4**, 873–884.

Fermi E. (1931) Über den Ramaneffekt des kolendioxyds. *Z. Phys.* **71**, 250–259.

Ferrero S., Bodnar R. J., Cesare B. and Viti C. (2010) Re-equilibration of primary fluid inclusions in peritectic garnet from metapelitic enclaves, El Hoyazo, Spain. *Lithos*. doi:10.1016/j.lithos.2010.09.004.

Fukura S., Mizukami T., Odake S. and Kagi H. (2006) Factors determining the stability, resolution, and precision of a conventional Raman spectrometer. *App. Spectr.* **60**, 946–950.

Goldstein R. H. and Reynolds T. J. (1994) Systematics of fluid inclusions in diagenetic minerals. *Soc. Sed. Geol. SEPM Short Course* **31**.

Gordon H. R. and McCubbin T. K. (1966) The 2.8-micron bands of CO_2. *J. Mol. Spectrosc.* **19**, 137–154.

Hollister L. S. (1981) Information intrinsically available from fluid inclusions. In *Fluid Inclusions: Applications to Petrology* (eds. L. S. Hollister and M. L. Crawford). *Min. Assoc. Can. Short Course*, vol. 6. pp. 1–12.

Izraeli E. S., Harris J. W. and Navon O. (1999) Raman barometry of diamond formation. *Earth Planet. Sci. Lett.* **173**, 351–360.

Kawakami Y., Yamamoto J. and Kagi H. (2003) Micro-Raman densimeter for the CO_2 inclusions in mantle-derived minerals. *App. Spectr.* **57**, 1333–1339.

Larson S. D. (1955) Phase studies of the two-component carbon dioxide–water system involving the carbon dioxide hydrate. Ph. D. diss., University of Illinois, Urbana, IL.

Lemmon E. W., McLinden M. O. and Friend D. G. (2010) Thermophysical properties of fluid systems. In *NIST Chemistry WebBook, NIST Standard Reference Database*, vol. 69 (eds. P. J. Linstrom and W. G. Mallard). National Institute of Standards and Technology, Gaithersburg, MD. Available from: <http://webbook.nist.gov>.

Lin F. and Bodnar R. J. (2010) Synthetic fluid inclusions XVIII: Experimental determination of the PVTX properties of H_2O–CH_4 to 500 °C, 3 kbar and $X_{CH4} \leqslant 4$ mol%. *Geochim. Cosmochim. Acta* **74**, 3260–3273.

Lin F., Bodnar R. J. and Becker S. P. (2007) Experimental determination of the Raman CH_4 symmetric stretching ($v1$) band position from 1–650 bar and 0.3–22 °C: application to fluid inclusion studies. *Geochim. Cosmochim. Acta* **71**, 3746–3756.

Mavrogenes J. A. and Bodnar R. J. (1994) Hydrogen movement into and out of fluid inclusions in quartz; experimental evidence and geologic implications. *Geochim. Cosmochim. Acta* **58**, 141–148.

McCreery R. L. (2000) *Raman Spectroscopy for Chemical Analysis*. John Wiley & Sons. 448 pp.

Roedder E. (1963) Studies of fluid inclusions II: freezing data and their interpretation. *Econ. Geol.* **58**, 167–211.

Roedder E. (1984) Fluid inclusions. In *Reviews in Mineralogy*, vol. 12 (ed. P. H. Ribbe). *Min. Soc. Am.*, Washington, DC.

Roedder E. and Bodnar R. J. (1997) Fluid inclusion studies of hydrothermal ore deposits. In *Geochemistry of Hydrothermal Ore Deposits* (ed. H. L. Barnes), third ed. Wiley & Sons Inc., New York, pp. 657–698.

Rosso K. M. and Bodnar R. J. (1995) Detection limits of CO_2 in fluid inclusions using microthermometry and laser Raman spectroscopy and the spectroscopic characterization of CO_2. *Geochim. Cosmochim. Acta* **59**, 3961–3975.

Schmidt C. and Bodnar R. J. (2000) Synthetic fluid inclusions: XVI. PVTX properties in the system H_2O–NaCl–CO_2 at elevated temperatures, pressures, and salinities. *Geochim. Cosmochim. Acta* **64**, 3853–3869.

Sloan E. D. and Koh C. A. (2008) *Clathrate hydrates of natural gases*, third ed. *Chem. Ind. Ser.*, vol. 119.

Song Y., Chou I. M., Hu W., Burruss R. and Lu W. (2009) CO_2 density-Raman shift relation derived from synthetic inclusions in fused capillaries and its application. *Acta Geol. Sinica* **83**, 932–938.

Span R. and Wagner W. (1996) A new equation of state for carbon dioxide covering the fluid region from the triple point temperature to 1100 K at pressures up to 800 MPa. *J. Phys. Chem. Ref. Data* **25**, 1509–1596.

Sterner S. M. and Bodnar R. J. (1984) Synthetic fluid inclusions in natural quartz I. Compositional types synthesized and applications to experimental geochemistry. *Geochim. Cosmochim. Acta* **48**, 2659–2668.

Sterner S. M. and Bodnar R. J. (1991) Synthetic fluid inclusions in natural quartz. X. Experimental determination of P–V–T–X properties in the CO_2–H_2O system to 6 kb and 700 °C. *Am. J. Sci.* **262**, 1055–1074.

Student J. J. and Bodnar R. J. (1999) Synthetic fluid inclusions XIV: microthermometric and compositional analysis of coexisting silicate melt and aqueous fluid inclusions trapped in the haplogranite–H_2O–NaCl–KCl system at 800 °C and 2000 bars. *J. Petrol.* **40**, 1509–1525.

Sun R. and Duan Z. H. (2005) Prediction of CH_4 and CO_2 hydrate phase equilibrium and cage occupancy from ab initio intermolecular potentials. *Geochim. Cosmochim. Acta* **69**, 4411–4424.

Takenouchi S. and Kennedy G. (1965) Dissociation pressures of the phase $CO_2 \cdot 5\frac{3}{4}H_2O$. *J. Geol.* **73**, 383–390.

Tattitch B. C., Candela P. A., Piccoli P. M., Bodnar R. J. and Fedele L. (2010) The effect of CO_2 on copper partitioning in a felsic melt–vapor–brine assemblage. *GSA Abstracts with Programs*, vol. 42. Paper No. 11–11.

Touret J. (1981) Fluid inclusions in high grade metamorphic rocks. In *Fluid Inclusions: Applications to Petrology* (eds. L. S. Hollister and M. L. Crawford). *Min. Assoc. Can. Short Course*, vol. 6. pp. 182–208.

Touret J. (2001) Fluids in metamorphic rocks. *Lithos* **55**, 1–25.

Wright R. B. and Wang C. H. (1973) Density effect on the Fermi resonance in gaseous CO_2 Raman scattering. *J. Chem. Phys.* **58**, 2893–2895.

Wright R. B. and Wang C. H. (1975) Effect of density on the Raman scattering of molecular fluids. II. Study of intermolecular interactions in CO_2. *J. Chem. Phys.* **61**, 2707–2710.

Yamamoto J. and Kagi H. (2006) Extended micro-Raman densimeter for CO_2 applicable to mantle-originated fluid inclusions. *Chem. Lett.* **35**, 610–611.

Yardley B. W. D. and Graham J. T. (2002) The origins of salinity in metamorphic fluids. *Geofluids* **2**, 249–256.

Associate editor: Zhenhao Duan